

# Unraveling multifractality and mobility edges in quasiperiodic Aubry-André-Harper chains through high-harmonic generation

Marlena Dziurawiec <sup>1</sup>, Jessica O. de Almeida <sup>2</sup>, Mohit Lal Bera <sup>2</sup>, Marcin Płodzień <sup>2</sup>, Maciej M. Maška <sup>1</sup>,  
Maciej Lewenstein <sup>2,3</sup>, Tobias Grass <sup>4,5,2</sup> and Utso Bhattacharya <sup>2</sup>

<sup>1</sup>*Institute of Theoretical Physics, Wrocław University of Science and Technology, 50-370 Wrocław, Poland*

<sup>2</sup>*ICFO - Institut de Ciències Fotòniques, Barcelona Institute of Science and Technology, 08860 Castelldefels (Barcelona), Spain*

<sup>3</sup>*ICREA, Passeig Lluis Companys 23, 08010 Barcelona, Spain*

<sup>4</sup>*DIPC - Donostia International Physics Center, Paseo Manuel de Lardizábal 4, 20018 San Sebastián, Spain*

<sup>5</sup>*IKERBASQUE, Basque Foundation for Science, Plaza Euskadi 5, 48009 Bilbao, Spain*



(Received 15 November 2023; accepted 3 July 2024; published 29 July 2024)

We show that high-harmonic spectroscopy offers an advanced avenue for probing electronic properties of quasicrystals beyond the linear response regime. Focusing on Aubry-André-Harper (AAH) chains, we extract the multifractal spectrum from the harmonic emission intensity—an essential indicator of the spatial distribution of electronic states in quasicrystals. Additionally, we address the detection of mobility edges, vital energy thresholds that demarcate localized and extended eigenstates within generalized AAH models. The precise identification of these mobility edges sheds light on the metal-insulator transition and the behavior of electronic states near these boundaries. Merging high-harmonic spectroscopy with the AAH model provides a powerful framework for understanding the interplay between localization and extended states in quasicrystals for an extremely wide energy range not captured within linear response studies, thereby offering valuable insights for guiding future experimental investigations.

DOI: [10.1103/PhysRevB.110.014209](https://doi.org/10.1103/PhysRevB.110.014209)

## I. INTRODUCTION

Investigating metal-insulator transitions is a fundamental inquiry within condensed matter physics. Anderson localization is a highly illustrative example of such transitions [1], where a system becomes an insulator due to disorder. To explore this type of transition, it is common to study disordered noninteracting models that display Anderson localization. However, simple one-dimensional Anderson models do not exhibit metal-insulator transitions, as they remain insulators regardless of the disorder strength. Recently, quasiperiodic systems have garnered significant attention as an alternative means to study localization and criticality. These models, unlike periodic or disordered systems, reveal nontrivial localization properties even in one spatial dimension. A well-known example demonstrating a metal-insulator transition in one dimension is the Aubry-André-Harper (AAH) model [2,3]. This model can be viewed in terms of the superposition of two incommensurate lattices. When one of the lattices is treated as a weak perturbation, an incommensurate quasiperiodic potential emerges. The AAH model has been experimentally realized in various setups, including ultracold atoms in optical lattices [4–9] and photonic devices [10], allowing researchers to gain deeper insight into the localization transition. See Appendix D for more details on the experimental implementation of the model.

For specific values of the quasiperiodic potential in the AAH model, a transition occurs between ergodic and localized states [11,12]. In practice, this transition can be observed in transport experiments by studying the dynamics of

particles or waves in these systems and measuring quantities such as diffusion, conductivity, or a few transport exponents. However, at the critical point, the spatial distribution of states shows different degrees of localization or delocalization across the system; as such, the system's behavior exhibits a wide range of different scaling behaviors or scaling exponents at different spatial scales. This behavior at the critical point of the AAH model, and also characteristic of other quasicrystalline systems such as the Fibonacci chain [13], is also called multifractality. While fractals are objects that can be characterized by a scaling law with one noninteger exponent, the fractal dimension, for a multifractal this is not enough to describe its dynamics. Instead, a continuous spectrum of exponents, or a singularity spectrum, is needed. Thus, determining multifractal behavior in quasiperiodic systems can be a very challenging task that has attracted strong attention in theoretical investigations [11,14,15], including also studies of intriguing consequences on the many-body phases [16]. Experimentally, the energy spectrum of a multifractal system has been achieved using cavity polaritons via photoluminescence [17].

Moreover, according to scaling theory, in one and two dimensions, infinitesimal random disorder leads to exponential localization of all single-particle states, resulting in the absence of diffusion [3]. However, in three-dimensional Anderson systems, localized and extended states can coexist at different energies. The critical energy level known as the single-particle mobility edge (SPME) separates localized and extended eigenstates in the energy spectrum [3,11]. Understanding the SPME is crucial in unraveling various fundamental phenomena, including metal-insulator

transitions and the thermoelectric response. Strikingly, some quasiperiodic systems can manifest localization phase transitions and SPMEs even in one dimension. The appearance of SPMEs is predicted by the continuous model of shallow quasiperiodic potentials [14–16]. However, in the presence of a tight-binding approximation, in the AAH model, because of the existence of a self-dual relation, the localization lengths of states remain independent of the energy, leading to the absence of an SPME. To generate SPMEs, short-range [18] or long-range hopping terms [19–21], spin-orbit coupling [22,23], or modified quasiperiodic potentials that violate the self-duality of the original AAH model [24–27] can be included to form a generalized AAH model. However, the observation of SPME requires high-resolution measurements of electronic states across a wide energy range. Therefore, experimental techniques with high sensitivity and resolution are essential.

In this paper, we show that evidence for fractal/multifractal properties of quantum states in real materials can be obtained from high-harmonic spectroscopy. This rapidly expanding field in strong-field attosecond science stands out for its great potential to uncover the structural, topological, and dynamical properties of materials [28,29]. High-harmonic generation (HHG) is a nonlinear optical process resulting from the interaction between an intense laser field and a material [30], gas [31–33], liquid [34–36], or crystal [37], producing high-order harmonics of the incident frequency. There has been a great deal of interest in HHG spectra in liquids due to their statistical effects, where the dynamics exhibits dephasing and the energy levels have a multiplateau structure [36]. The same energy band structure is observed in the HHG of nonlocalized electrons in crystals [38,39]. HHG allows for the generation of high-frequency harmonics, enabling probing of a broad energy range in the electronic band structure, including states near the mobility edge. Recently, HHG spectroscopy has been proposed as a modern tool for probing the topological phases of matter [40–44]. Furthermore, HHG is also sensitive to electronic wave functions and their spatial distribution [45].

By analyzing the nonlinear optical response of 1D quasicrystals, we show that HHG spectroscopy can reveal information about the localization and multifractal properties of states. Specifically, the three main results of our work are as follows: (i) HHG can distinguish between localized and extended states, even if the energy spectra in both cases are identical, (ii) HHG is suited to identify and characterize multifractal states, and (iii) HHG can identify the localization edge. Hence, a rich picture of the properties of a quasicrystal can be obtained from HHG, combining insights that are traditionally derived from energy spectra measurements and transport studies.

## II. MODEL

Specifically, our study concentrates on quasicrystals described by the AAH model from the point of view of high-harmonic spectroscopy. By analyzing the intensity of the harmonics emitted, we demonstrate the potential to obtain the entire multifractal spectrum or distribution, which reveals crucial information about the localization properties of electronic states in these quasicrystals. Beyond multifractal analysis, our

research delves into the detection of mobility edges in generalized AAH models. We show that high-harmonic spectra can serve as a powerful tool for identifying critical energy points that separate localized and extended eigenstates. This provides valuable insights into the metal-insulator transition and the behavior of electronic states around the mobility edge. Through the combination of high-harmonic spectroscopy with the AAH model, our theoretical study sheds light on the intricate interplay between localization and extended states in quasicrystals.

The AAH model [2,3] is given by the Hamiltonian

$$\hat{H} = -J \sum_{j=1}^N (c_j^\dagger c_{j+1} + c_{j+1}^\dagger c_j) + 2V \sum_{j=1}^N \cos(2\pi\beta j) c_j^\dagger c_j, \quad (1)$$

where  $J$  is the hopping strength between nearest-neighbor sites and  $2V$  is the amplitude of the on-site potential. Parameter  $\beta$ , an irrational number modulating lattice periodicity, is chosen as the golden ratio  $(\sqrt{5} - 1)/2$ , approximated by  $\beta \approx \text{Fibonacci}(n+1)/\text{Fibonacci}(n)$  with the number of lattice sites  $N = \text{Fibonacci}(n)$ . For the results presented here, we set  $N = 610 = \text{Fibonacci}(15)$ . The creation (annihilation) operators,  $c_j^\dagger$  ( $c_j$ ), create (annihilate) a spinless (or spin polarized) electron on lattice site  $j$ , and the upper limit of the sum in the hopping term  $N$  instead of  $N - 1$  implies periodic boundary conditions. In Appendix B we demonstrate that the size of the system is sufficient to demonstrate all the main properties of the HHG spectrum.

For a dominant on-site potential,  $V > J$ , the single-particle electronic wave functions are localized, i.e., concentrated to certain lattice sites, and the material behaves as an insulator, as in the Anderson model with negligible contribution to charge transport. Whereas, when nearest-neighbor hopping is dominant,  $J > V$ , the electrons are delocalized, i.e., grossly uniformly distributed at all lattice sites and can exhibit charge transport in the presence of an infinitesimal electric field, thus behaving as a metal. By implementing a duality transformation of the form  $c_k^{(\dagger)} = \frac{1}{\sqrt{N}} \sum_j e^{\pm i2\pi\beta k j} c_j^{(\dagger)}$  for the AAH model, a critical point,  $V = J$ , can be identified where the model is self-dual and exhibits multifractal properties [2,46–48]. The effect of this transformation is to go to a momentum-space-like representation where wave functions that are delocalized in real space are localized in the dual space and vice versa. This is true except at the critical point, where the wave functions are localized and delocalized simultaneously in both spaces, thus exhibiting multifractal behavior. The duality relation also establishes a remarkable equivalence of energy levels in the AAH model: for a given choice of parameter,  $V/J = \alpha$ , and for its inverse,  $V/J = \alpha^{-1}$ , the energy levels are identical. Despite the identical energies, the single-particle states differ significantly, as these regions belong to distinct phases with opposite localization profiles.

## III. COUPLING WITH LIGHT

We now couple the AAH model with a strong linearly polarized incident laser pulse. Our objective is to analyze the HHG spectrum, obtained via a windowed Fourier transform of the time-dependent lattice current operator, and identify

quantitative indicators of localized and delocalized phases within the AAH model. The HHG spectra carry crucial information about both the energy levels and the eigenstates of the system.

In the regime where the laser wavelength is much larger than the length of the system, the laser field coupling is well represented by the dipole approximation. The incident laser vector potential and electric field are

$$\vec{A}(t) = A(t)\hat{x}, \quad \vec{E}(t) = -\partial_t \vec{A}(t). \quad (2)$$

In the velocity gauge, the light-matter coupling induces a phase difference in the electronic hopping, dependent on the distance between neighbor sites, the Peierls phase,  $\vec{A} \cdot (\vec{r}_n - \vec{r}_{n'})$ , and therefore the time-dependent hopping amplitude is

$$J(t) = J e^{ie(n-n')A(t)/\hbar} = J e^{ieA(t)/\hbar}, \quad (3)$$

where  $e$  is the electron charge and we assume the lattice constant  $a = 1$ . The distance is given in units of lattice constants and  $A(t)$  is a time-dependent vector potential that describes the shape of the laser pulse,

$$A(t) = A_0 \sin^2\left(\frac{\omega_0 t}{2n_c}\right) \sin(\omega_0 t), \quad 0 < t < \frac{2\pi n_c}{\omega_0}. \quad (4)$$

The number of cycles is  $n_c = 5$ , and the laser field frequency is  $\omega_0 = 0.004$  with amplitude  $A_0 = 0.4$ .

The time-dependent Hamiltonian of the generalized AAH model is

$$\begin{aligned} \hat{H}(t) = & \sum_{j=1}^N (J(t)c_j^\dagger c_{j+1} + \text{H.c.}) \\ & + 2V \sum_{j=1}^N \frac{\cos(2\pi\beta j)}{1 - b \cos(2\pi\beta j)} c_j^\dagger c_j. \end{aligned} \quad (5)$$

The motion of the carriers within the bands creates a macroscopic current observable, with the current operator in the velocity gauge [41,49],

$$\hat{I}(t) = i \sum_{j=1}^N (J(t)c_j^\dagger c_{j+1} - J^*(t)c_{j+1}^\dagger c_j), \quad (6)$$

and the expectation value is given by

$$I(t) = \sum_{j=1}^v \langle \psi_j(t) | \hat{I}(t) | \psi_j(t) \rangle, \quad (7)$$

where  $v$  is the number of particles in the system (filling), and  $|\psi_j(t)\rangle$  is the time evolution of each occupied single-particle energy state from  $t = 0$ . Using the Crank-Nicolson approximation, the time evolution of the wave function is calculated as follows,

$$\begin{aligned} |\Psi(t + \delta t)\rangle &= \exp[-i\mathcal{H}(t)\delta t] |\Psi(t)\rangle \\ &\approx \frac{1 - i\mathcal{H}(t + \delta t/2)\delta t/2}{1 + i\mathcal{H}(t + \delta t/2)\delta t/2} |\Psi(t)\rangle, \end{aligned} \quad (8)$$

with time step  $\delta t$  and initial state  $|\psi_j(t = 0)\rangle$  that is the  $j$ th eigenvector of the Hamiltonian (10).

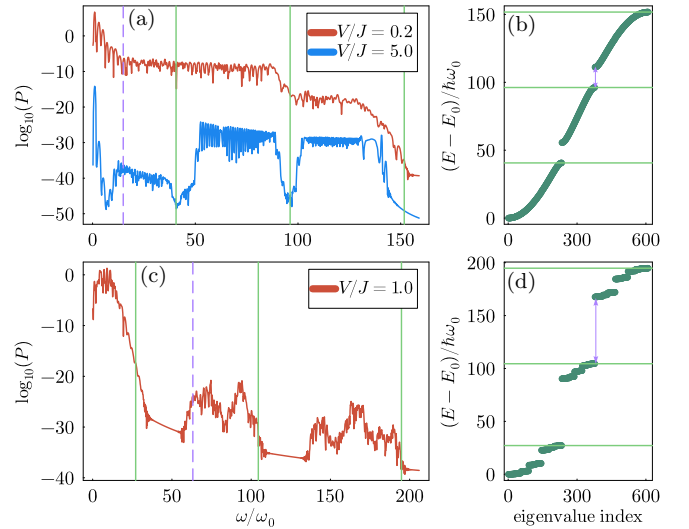


FIG. 1. (a) The HHG spectra for extended ( $V/J = 5^{-1}$ ) and localized ( $V/J = 5$ ) phases. In the extended phase  $J = 0.15 \approx 40\hbar\omega_0$  (red) and in the localized phase  $V = 0.15 \approx 40\hbar\omega_0$  (blue). The system is half filled. (b) Corresponding energy spectra for both phases (overlapping). (c) and (d) The same as in panels (a) and (b), but for  $V/J = 1$ .

The Fourier transform of the derivative of the time-dependent current is proportional to the emitted radiation in the frequency domain,

$$P(\omega) = |\text{FFT}[\dot{I}(t)]|^2. \quad (9)$$

#### IV. LOCALIZATION-DELOCALIZATION

In Fig. 1(a), we present the high harmonic emitted from the interaction of a pulse laser field with a system in the AAH model for  $V/J = 5^{-1}$  and  $V/J = 5$ . For comparison, Fig. 1(b) shows the energy spectrum which is identical for both phases. Despite the equal energy levels, the high-harmonic spectra are crucially different, with a magnitude difference in the emission power for the two phases, highlighting the sensitivity of the HHG spectrum to the spatial structure of the eigenstates. The spectra of the extended phase (in red) exhibit metallic behavior with high emission power. In contrast, the localized phase (in blue) has features of insulating materials. In stark contrast to HHG in noninteracting semiconductors, where the HHG spectrum shows metallic or insulating behavior depending on the filling of a band, the high-harmonic spectrum from the AAH model does not depend on the filling, as either all single-particle states are completely localized or delocalized for a given value of the model parameters. Importantly, the HHG spectrum also carries useful information about the energy spectrum, in particular the position of the band edges. This is most pronounced in the localized phase (blue curve), where the HHG spectrum has dips/cutoffs [vertical green lines in Fig. 1(a)]. These coincide with the band edges in the energy spectrum [horizontal green lines in Fig. 1(b)]. The origin of this coincidence is most obvious for the highest one: The corresponding energy equals the total bandwidth of the system and no emission is possible at higher frequencies. Similarly, the edges of the other band also define frequencies

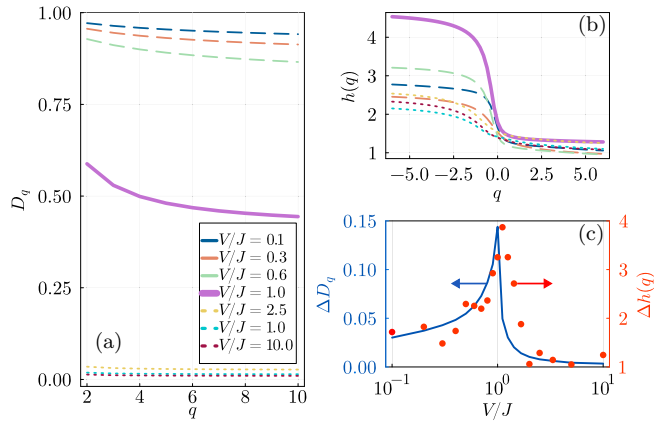


FIG. 2. (a) Fractal dimension as a function of  $q$ . (b) Hurst exponent as a function of  $q$ . (c) Width of curves  $D_q$  (line) and  $h(q)$  (dots) comparing a multifractality of the eigenstates and HHG spectra.

at which the emission probability is reduced by the spectral gap. Since interband processes require energy higher than the emission below the gap, only intraband transitions can contribute to the emission. As a result, the size of the energy gap [marked by the purple line in Figs. 1(a) and 1(b)] corresponds to a frequency in the HHG spectrum below which emission is suppressed.

## V. MULTIFRACTALITY

At the critical point,  $V = J$ , the AAH model shows characteristic features common to both localized and delocalized phases, thus presenting multifractal behavior. We show the high harmonic and energy spectrum for the multifractal point in Figs. 1(c) and 1(d). Again, the green lines in these plots demonstrate a relation between cutoffs in the HHG spectrum and band edges in the energy spectrum. Now, the energy spectrum has a fractal structure with splitting of the bands into subbands separated by smaller gaps. Notably, such a structure is also observed in the HHG signal. Again, the purple line in Figs. 1(c) and 1(d) shows that also information about the size of the largest energy gap is reflected in the HHG spectrum. While it might be hard to resolve also smaller gaps, we show that the degree of localization of eigenstates and the multifractal spectrum can directly be read out from the harmonic spectrum by using multifractal detrended fluctuation analysis (MF-DFA). Therefore, the HHG spectrum of a multifractal system complements measurements of bare energy spectra.

The standard measure that quantifies the  $q$  fractality of a quantum state is the multifractal dimension  $D_q$  [50,51]. A completely localized state has dimension  $D_q \approx 0$ , while a completely delocalized state has dimension  $D_q \approx 1$ , and in both cases  $D_q$  is nondispersive. Figure 2(a) shows  $D_q$  for the AAH model for different ratios  $V/J$ . At the critical point  $V = J$ ,  $D_q$  varies around 0.5 and is dispersive with  $q$ , indicating multifractality. Multifractals have multiple scaling exponents, so that their fractal dimension depends on  $q$ . Thus, to quantify the nature of the eigenstates, we define  $\Delta D_q \equiv \max(D_q) - \min(D_q)$  which is maximal at the multifractal point, while it is close to zero in the localized and delocalized phases, as illustrated in Fig. 2(c).

Now, we analyze dynamical indicators of multifractality. In particular, we will show that multifractality also manifests itself in the nonlinear optical response. To this end, we demonstrate that the generalized Hurst exponent  $h(q)$  [52] characterizing the high-harmonic spectrum is closely related to the multifractal dimension  $D_q$  of the AAH eigenstates.  $h(q)$  is typically used as a measure of the long-term memory of a time series. Here, instead of in the time domain, we calculate it in the frequency domain. As explained in detail in Appendix A, this exponent can be extracted from the power spectrum of HHG. This means that in our case  $h(q)$  quantifies how rapidly the correlations between the emitted power decrease as the distance between frequencies increases. We observe that for monofractals  $h(q)$  is almost constant, while for multifractals it strongly depends on  $q$ . As shown in Fig. 2(b) for different  $V/J$ ,  $h(q)$  is constant for both  $q < 0$  and  $q > 0$ , with a jump around  $q = 0$ . Importantly, the magnitude of this jump increases as we approach the multifractal point  $V = J$ . Then, similarly to  $D_q$ ,  $\Delta h(q) \equiv \max[h(q)] - \min[h(q)]$  for multifractals is greater than for monofractals and allows one to quantify multifractality. The red dots in Fig. 2(c) show that  $\Delta h(q)$  has a peak for values  $V/J$  close to the critical point that closely resembles the behavior of  $\Delta D_q$ . This comparison clearly indicates that  $h(q)$  is interconnected with the fractal dimension  $D_q$ , which, in turn, demonstrates that the static multifractal features of eigenstates can be decoded from the HHG spectrum using the MF-DFA technique.

## VI. MOBILITY EDGE

We next turn to the study of mobility edges, i.e., critical energies that sharply separate localized and delocalized states for fixed system parameters. While the original AAH Hamiltonian does not exhibit a mobility edge at finite energy, such a feature appears already in simple generalizations of the AAH Hamiltonian. For concreteness, we choose

$$\hat{H} = \sum_{j=1}^N (Jc_j^\dagger c_{j+1} + J^* c_{j+1}^\dagger c_j) + 2V \sum_{j=1}^N \frac{\cos(2\pi\beta j)}{1 - b \cos(2\pi\beta j)} c_j^\dagger c_j, \quad (10)$$

where for any value of  $b \neq 0$  the system shows a mobility edge, as this term breaks the self-duality relation in the model [53]. Notably, there exists an analytical solution that yields the relation of the mobility edge with the hopping strength and the on-site potential [53,54].

A key quantity that can identify mobility edges between localized and delocalized states is the inverse participation ratio  $\text{IPR}(v) = \sum_i |\psi_{v,i}|^4$ , where  $\psi_{v,i}$  is a component of the  $v$ th eigenstate  $|\Psi_v\rangle = |\psi_{v,1}, \psi_{v,2}, \dots, \psi_{v,L}\rangle$  localized on the  $i$ th lattice site [55].

A zero IPR is a signature of delocalization, whereas a unit IPR represents localization. A sharp change in IPR indicates the presence of a mobility edge. Subsequently, we show how the energy spectra and IPR of each eigenstate vary with  $V/J$ , for zero and nonzero  $b$ , and how this behavior of IPR can also be captured directly in HHG.

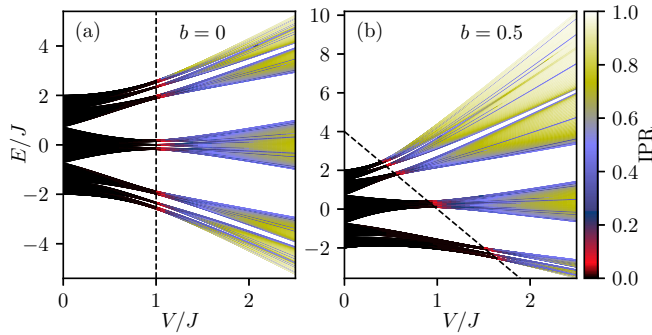


FIG. 3. Energy levels of Hamiltonian (10) as a function of  $V/J$  (a) in the absence of SPME ( $b = 0$ ) and (b) in the presence of SPME ( $b = 0.5$ ). Colors represent the IPR of the corresponding eigenstate. For eigenstates to the left of the dashed line IPR = 0. For  $b = 0.5$  its analytic form is  $E/J = 4 - 4V/J$  [53].

We illustrate this in Fig. 3, where the energy spectrum versus  $V/J$  is shown for two cases where  $b = 0$  and  $b = 0.5$ . The colors represent the IPR of the corresponding eigenstates. For  $b = 0$  we observe a symmetric energy spectrum with IPR that depends only on  $V/J$ , but not on the energy (or filling). Thus, depending on the modulation amplitude, the eigenstates are either all localized or all delocalized, which indicates the absence of the mobility edge. For  $b \neq 0$  the energy spectrum is asymmetric and the IPR shows a filling-dependent behavior typical for energy spectra with the mobility edge. To examine whether the HHG spectra can show a signature of mobility edges, we time-evolve the model while changing the filling  $\nu$  as described in Sec. III. In Fig. 4 we compare the spectra in two cases,  $b = 0$  and  $b = 0.5$  for  $V/J = 0.3$  and  $V/J = 1$ . As can be seen in Fig. 3, for  $V/J = 0.3$  all eigenstates are delocalized, and therefore the HHG spectra are similar. However, in proximity to a critical point for  $V/J = 1$ , the spectra differ significantly. As a rule of thumb, we find that the differences in the high-harmonic spectrum originate from differences in the energy spectrum if the harmonics correspond to energies higher than the band gap of the system. However, contributions below the band gap strongly depend on the filling, which is connected with the existence of the mobility edges. To quantify this observation, we introduce a logarithm of the

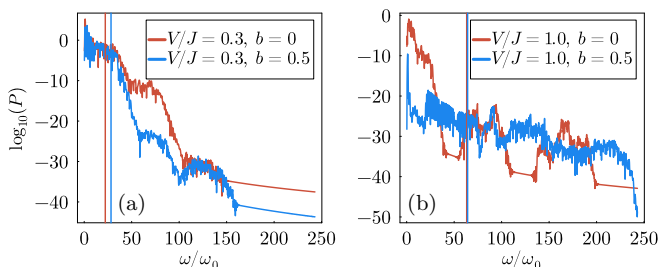


FIG. 4. Examples of the HHG spectra for  $V/J = 0.3$  (a) and  $V/J = 1$  (b) for  $b = 0$  (red line) and  $b = 0.5$  (blue line). For  $V/J = 0.3$  all eigenstates are delocalized and both spectra are similar. For  $V/J = 1$  eigenstates are localized for  $b = 0$ , but there is SPME for  $b = 0.5$ . Vertical lines indicate the largest gap  $\Delta E/\hbar\omega_0$  between energy levels. These plots are for filling given by occupation of 450 lowest states (out of 610).

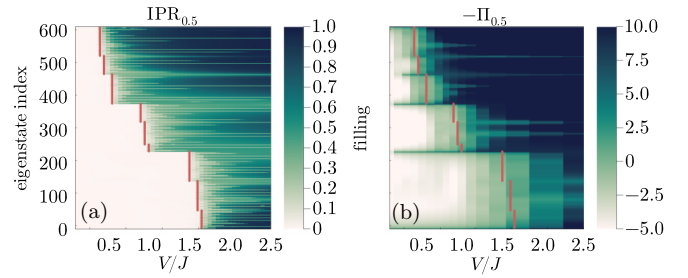


FIG. 5. Comparison of IPR (a) and  $-\Pi$  (b) for the case where the SPME is present in the energy spectrum ( $b = 0.5$ ).  $\nu$  is the eigenstate number. Red points indicate the mobility edge calculated analytically [53].

total power emitted in frequencies below the largest gap in the energy spectrum  $\Delta E_b/\hbar$  (marked by vertical lines in Fig. 4),

$$\Pi_b = \log_{10} \int_0^{\Delta E_b/\hbar} P_b(\omega) d\omega, \quad (11)$$

where  $P_b(\omega)$  denotes the density of power emitted at frequency  $\omega$  for the AAH model [see (9)]. The index  $b$  indicates that the corresponding quantities were calculated for this particular value of parameter  $b$  in the potential in Hamiltonian (10). Limiting the frequencies to  $\Delta E/\hbar$  means that  $\Pi_b$  is dominated by intraband contributions [56].

In Fig. 5 we compare this quantity with the IPR for a model with SPME ( $b = 0.5$ ). The comparison shows a striking similarity between  $\Pi$  and IPR. It can be seen that the critical value of  $V/J$  that separates the extended and localized states corresponds to a jump in the below-band-gap contribution of the HHG spectrum defined in Eq. (11). The behavior of these two quantities is opposite; that is, IPR for extended states is smaller than for localized states, whereas the opposite is true for  $\Pi$ . Therefore, to emphasize the similarity of the qualitative behavior, in Fig. 5(b) we present  $-\Pi$ . The threshold is not as sharp as in the case of IPR, but IPR, in contrast to  $\Pi$ , is not directly accessible in experiments. By comparing  $\Pi$  with the analytical result for the SPME given in Ref. [53], we conclude that the criterion for localization is  $\Pi \approx 2.5$ . In this way, we have shown that the mobility edge can be detected solely from the high-harmonic spectra below the band gap.

Characterization of the entire multifractal spectrum and detection of mobility edges pose significant experimental challenges for quasiperiodic systems. The results presented here address these problems through the lens of HHG and pave the way for future experimental investigations, contributing to a deeper understanding of the multifractality and mobility edges in quasicrystals and their potential applications in condensed matter physics.

## ACKNOWLEDGMENTS

ICFO group acknowledges support from European Research Council AdG NOQIA; MCIN/AEI (PGC2018-0910.13039/501100011033, CEX2019-000910-S/10.13039/501100011033, Plan National FIDEUA PID2019-106901GB-I00, Plan National STAMEENA PID2022-139099NB, I00, project funded by MCIN/AEI/10.13039/501100011033 and by the “European

Union NextGenerationEU/PRTR” (PRTR-C17.I1), FPI); QUANTERA MAQS (PCI2019-111828-2); QUANTERA DYNAMITE PCI2022-132919, QuantERA II Programme co-funded by European Union’s Horizon 2020 program under Grant Agreement No. 101017733; Ministry for Digital Transformation and of Civil Service of the Spanish Government through the QUANTUM ENIA project call - Quantum Spain project, and by the European Union through the Recovery, Transformation and Resilience Plan - NextGenerationEU within the framework of the Digital Spain 2026 Agenda; Fundació Cellex; Fundació Mir-Puig; Generalitat de Catalunya (European Social FundFEDER and CERCA program, AGAUR Grant No. 2021 SGR 01452, QuantumCAT \ U16-011424, co-funded by ERDF Operational Program of Catalonia 2014-2020); Barcelona Supercomputing Center MareNostrum (FI-2023-3-0024); Funded by the European Union. Views and opinions expressed are however those of the author(s) only and do not necessarily reflect those of the European Union, European Commission, European Climate, Infrastructure and Environment Executive Agency (CINEA), or any other granting authority. Neither the European Union nor any granting authority can be held responsible for them (HORIZON-CL4-2022-QUANTUM-02-SGA PASQunS2.1, 101113690, EU Horizon 2020 FET-OPEN OPTologic, Grant No. 899794), EU Horizon Europe Program (This project has received funding from the European Union’s Horizon Europe research and innovation program under Grant Agreement No. 101080086 NeQSTGrant Agreement 101080086–NeQST); ICFO Internal “QuantumGaudi” project; European Union’s Horizon 2020 program under the Marie Skłodowska-Curie Grant Agreement No. 847648 “La Caixa” Junior Leaders fellowships, “La Caixa” Foundation (ID 100010434) CF/BQ/PR23/11980043. M.M.M. acknowledges that this research is part of the Project No. 2021/43/P/ST3/03293 co-funded by the National Science Centre and the European Union’s Horizon 2020 research and innovation program under the Marie Skłodowska-Curie Grant Agreement No. 945339. M.D. acknowledges support from the National Science Centre (Poland) under Grant No. 2022/04/Y/ST3/00061. M.P. acknowledges the support of the Polish National Agency for Academic Exchange, the Bekker program, Grant No. PPN/BEK/2020/1/00317.

The BBVA Foundation takes no responsibility for the opinions, statements, and contents of this project, which are entirely the responsibility of its authors. As well, the views and opinions expressed are those of the authors only and do not necessarily reflect those of the European Union, European Commission, European Climate, Infrastructure, and Environment Executive Agency (CINEA), or any other granting authority. Neither the European Union nor any granting authority can be held responsible for them.

## APPENDIX A: MULTIFRACTAL DETRENDED FLUCTUATION ANALYSIS

The challenging theoretical problem of quantum localization of excitations in disordered systems has greatly advanced since Anderson’s [1] initial paper. It has been discovered that the transition between localization and delocalization induced

by disorder is characterized by intricate spatial patterns in wave functions. This pattern is believed to have a multifractal structure at the localization threshold. A similar behavior is known to be also present in the AAH model, studied in this work.

The quantity commonly used to study the localization/delocalization transition is the inverse participation ratio (IPR) defined in the main text. For critical eigenstates, the IPR follows an anomalous scaling with the system size that depends on their multifractal dimension  $D_q$  [57]. Moreover,  $D_q$  can be used directly to quantify the degree of localization of the wave function [50,51]. It can be calculated by partitioning the  $\nu$ th eigenstate  $|\Psi_\nu\rangle$  into  $M$  segments of size  $l$  and calculating the generalized mean of cumulative probability in each segment,

$$D_q(|\Psi_\nu\rangle) = \frac{1}{q-1} \frac{\ln \left[ \sum_{k=0}^{M-1} \left( \sum_{j=1}^l |\psi_{\nu,kl+j}|^2 \right)^q \right]}{\ln(M^{-1})}, \quad (\text{A1})$$

where  $|\Psi_\nu\rangle = |\psi_{\nu,1}, \psi_{\nu,2}, \dots, \psi_{\nu,L}\rangle$  is an eigenstate written in the position basis,  $l = 4$ , and  $M = \lfloor L/l \rfloor$ . In the main text, we demonstrate that this quantity can be estimated from the optical response. That is, we relate it to the generalized Hurst exponent  $h(q)$  of the HHG spectrum. In the following, we briefly describe how it can be calculated in the framework of multifractal detrended fluctuation analysis (MF-DFA) [52]. The MF-DFA is an extension that enhances the conventional detrended fluctuation analysis (DFA) to handle nonstationary time series exhibiting multifractal scaling characteristics. By examining the local scaling of fluctuations in relation to smooth trends across segmented polynomial fits, the MF-DFA enables precise estimation of the multifractal parameters of a signal, such as its multifractal spectrum. In our analysis, the multifractal signal depends on frequencies rather than time.

First, we obtain the series profile—we calculate a cumulative sum of a mean-centered data,

$$y(\omega) = \int_0^\omega [\log_{10} P(\omega') - \langle \log_{10} P \rangle] d\omega', \quad (\text{A2})$$

where  $\langle \log_{10} P \rangle$  is the arithmetic mean. Through the MF-DFA calculations we use the data up to 200th harmonic. The curve  $y(\omega)$  is then divided into segments (“boxes”) of size  $s$ , with  $N_s$  being the total number of segments. In the next step, each  $y_\nu(\omega)$  [part of  $y(\omega)$  that is inside the segment  $\nu = 1, 2, \dots, N_s$ ] is being fitted with a second-order polynomial  $\bar{y}_\nu(\omega)$ , so we calculate local trends. We have verified that using higher-order polynomials does not give a better agreement between results obtained from the HHG spectra and those calculated directly from the wave functions. We remove the trends by subtracting the fitting from the respective data part  $y_\nu(\omega)$ , then we calculate the variance for each segment,

$$F_\nu^2(s) = \frac{1}{s} \int_{(\nu-1)s}^{\nu s} [y_\nu(\omega) - \bar{y}_\nu(\omega)]^2 d\omega. \quad (\text{A3})$$

Next, we obtain the generalized mean (power mean) of a variance over all segments, see Fig. 6 for an example,

$$F_q(s) = \left\{ \frac{1}{N_s} \sum_{\nu=1}^{N_s} [F_\nu^2(s)]^{q/2} \right\}^{1/q}. \quad (\text{A4})$$

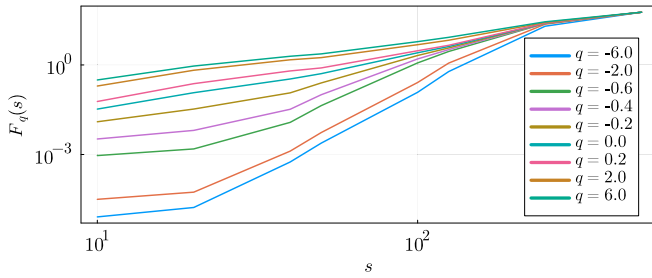


FIG. 6. Example of  $F_q(s)$  [see Eq. (A4)] behavior for  $V/J = 1.25$  and several values of  $q$ .

The calculations are repeated for various segment sizes  $s$ , ranging from  $2\omega_0$  to  $100\omega_0$ , with a fixed exponent  $q$ . Then, the curve  $F_q(s)$  is fitted with a power law,  $F_q(s) \propto s^{h(q)}$ . The exponent  $h(q)$  is a generalized exponent, closely related to the generalized Hurst exponents  $H(q)$ ;  $H(q) = h(q) - 1$  for  $h(q) > 1$ .

### APPENDIX B: FINITE-SIZE EFFECTS

The requirement that the system size be a Fibonacci number makes it difficult to perform finite-size scaling. In particular, the time evolution of the wave functions would be challenging for a very large system. Since some of the results are for half filling, we need the number of eigenstates (and so the number of lattice sites) to be an even number. The main results of this work have been obtained for size 610 [Fibonacci(15)]; the next even Fibonacci number is 2584. Fortunately, by comparing the current results with those obtained for a smaller system, we can show that the current system size already guarantees the convergence of the high-harmonic spectrum and the quantities we calculate from it. Figure 7 shows a direct comparison of the spectra for systems with 144 and 610 lattice sites, whereas Fig. 8 shows the same as Fig. 2(c), but also for a system with 144 lattice sites. These figures demonstrate that the HHG spectra depend only quantitatively on the size of the system with all the characteristic features located at precisely the same frequency for 144 and 610 lattice sites. The energy spectra are almost identical; the same is true for the position of the maximum in  $\Delta D_q$  and  $\Delta h(q)$  which indicates the multifractal point.

### APPENDIX C: HIGHER LASER FREQUENCY

It is possible to reduce the number of harmonic orders that is necessary to observe the full spectrum up to the cutoff, by using a higher laser frequency. However, it also reduces the resolution of the obtained spectra. Here we present effects of a frequency 5 times higher than in the main part of the paper ( $\omega_0 = 0.02$ ) which results in the cutoff of the order  $\sim 30$  harmonics. The localized and extended phases can be distinguished through HHG spectra and most of the characteristic features of the spectrum in the insulating phase are still preserved, as shown in Fig. 9. The SPMEs can also be observed by the method described in the paper, but in this case the results are more affected by noise, especially for low values of  $V/J$ ; see Fig. 10. However, we report that for the

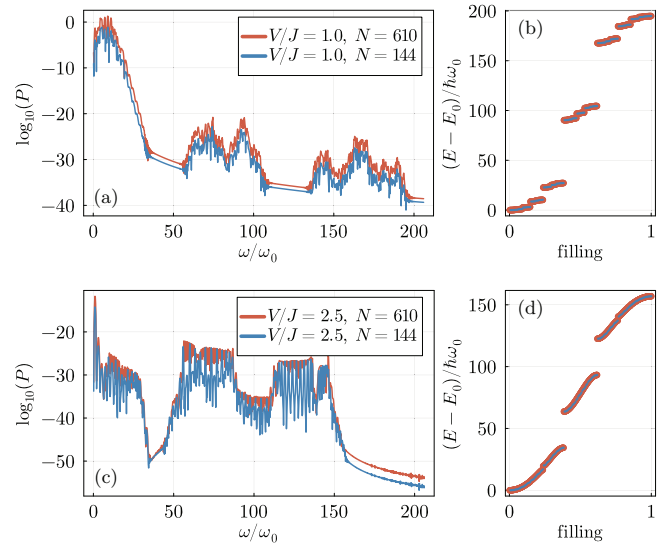


FIG. 7. Comparison of the HHG spectra for  $V/J = 1$  (a) and  $V/J = 2.5$  (c) for systems with 610 (red line) and 144 (blue line) lattice sites. The corresponding energy spectra are shown in panels (b) and (d), respectively. Since the energy spectra are presented for different system sizes, the eigenvalue numbers were normalized and denoted as “filling” on the horizontal axis in panels (b) and (d).

correct multifractality predictions via the MF-DFA analysis, a higher resolution is needed.

### APPENDIX D: EXPERIMENTAL IMPLEMENTATION

Finally, let us discuss some experimental implications of our theoretical study of HHG as a detection tool for multifractality and mobility edges in the quasiperiodic Aubry-André-Harper chain. Obviously, our study applies immediately to 1D models in the context of synthetic quasicrystals, such as AAH chains implemented in atomic or photonic platforms (see [4–10]). However, 1D quasicrystals also serve as building blocks of quasicrystalline systems in two or three dimensions, see in this context Ref. [13] for a review on the Fibonacci chain, with similar multifractal behavior as the critical AAH chain. Three-dimensional quasicrystals were discovered in aluminum-manganese alloys in the 1980s [58].

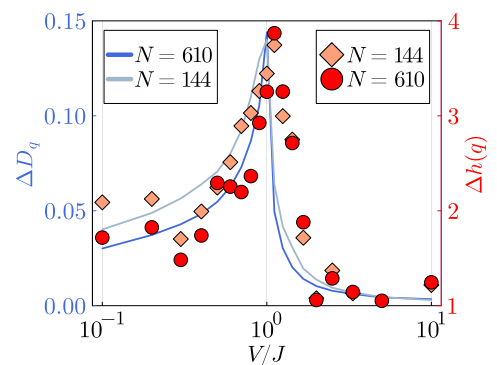


FIG. 8. The same as Fig. 2(c), but for systems with 144 and 610 lattice sites.

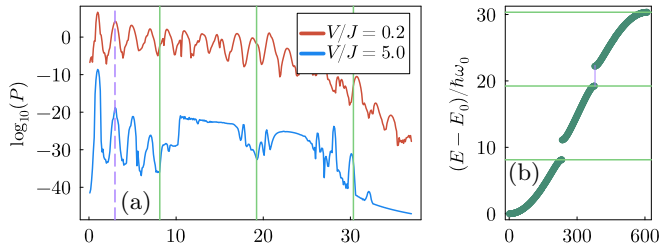


FIG. 9. (a) The HHG spectra with the laser parameters  $n_c = 10$ ,  $\omega_0 = 0.02$  for extended ( $V/J = 5^{-1}$ ) and localized ( $V/J = 5$ ) phases. The system is half filled. (b) Corresponding energy spectra for both phases (overlapping).

Systems beyond 1D are of particular interest in our context because the efficiency of HHG depends on the number of electrons involved in the emission process. For an estimate of the efficiency, we will consider two cases here: (i) an array of noninteracting 1D chains, like in this paper; (ii) a truly 2D quasicrystal.

(i) *1D estimation.* We can consider 2000 chains of the length 10 000 on a substrate. More generally, stacking a layer of active material on a substrate with different periodicity could automatically generate quasiperiodic coupling. This can be achieved using standard magnetic beam epitaxy, or better, van der Waals materials, as is done in twistronics [59–61]. We could thus have 10 000 electrons, filling the lowest

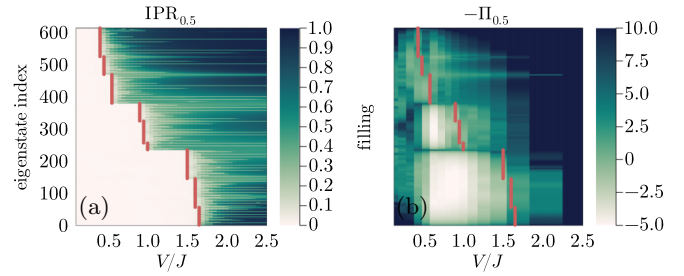


FIG. 10. Comparison of IPR (a) and  $-\Pi$  (b) for  $\omega_0 = 0.02$ ,  $n_c = 10$  and the case where the SPME is present in the energy spectrum ( $b = 0.5$ ).  $\nu$  is the eigenstate number. Red points indicate the mobility edge calculated analytically [53].

band, but in different orbitals. We estimate optimistically-conservatively they will contribute as 5000 (half of their number). All of them should be phase matching because of the regular spatial arrangements. This gives a factor of  $10^8$ . This means that the signal of Fig. 4 for many-particle response will be a factor  $10^{16}$  higher. Conversion efficiency (see Figs. 1 and 4) will then reach  $10^{-6}$  to  $10^{-4}$ , comparable to HHG in atomic clouds or solids. This is an optimistic estimate but is not so far from a feasible experimental truth.

(ii) *2D estimation.* Here clearly lattices of  $10\,000 \times 2000$  are possible. Thus, a 2D model is expected to be the same/similar to that we studied here.

- [1] P. W. Anderson, Absence of diffusion in certain random lattices, *Phys. Rev.* **109**, 1492 (1958).
- [2] S. Aubry and G. André, Analyticity breaking and Anderson localization in incommensurate lattices, *Ann. Israel Phys. Soc.* **3**, 133 (1980).
- [3] P. G. Harper, Single band motion of conduction electrons in a uniform magnetic field, *Proc. Phys. Soc. A* **68**, 874 (1955).
- [4] H. P. Lüschen, S. Scherg, T. Kohlert, M. Schreiber, P. Bordia, X. Li, S. Das Sarma, and I. Bloch, Single-particle mobility edge in a one-dimensional quasiperiodic optical lattice, *Phys. Rev. Lett.* **120**, 160404 (2018).
- [5] G. Modugno, Anderson localization in Bose-Einstein condensates, *Rep. Prog. Phys.* **73**, 102401 (2010).
- [6] G. Roati, C. Errico, L. Fallani, M. Fattori, C. Fort, M. Zaccanti, G. Modugno, M. Modugno, and M. Inguscio, Anderson localization of a non-interacting Bose-Einstein condensate, *Nature (London)* **453**, 895 (2008).
- [7] M. Lohse, C. Schweizer, O. Zilberberg, M. Aidelsburger, and I. Bloch, A Thouless quantum pump with ultracold bosonic atoms in an optical superlattice, *Nat. Phys.* **12**, 350 (2016).
- [8] S. Nakajima, T. Tomita, S. Taie, T. Ichinose, H. Ozawa, L. Wang, M. Troyer, and Y. Takahashi, Topological Thouless pumping of ultracold fermions, *Nat. Phys.* **12**, 296 (2016).
- [9] F. An, K. Padavić, E. Meier, S. Hegde, S. Ganeshan, J. Pixley, S. Vishveshwara, and B. Gadway, Interactions and mobility edges: Observing the generalized Aubry-André model, *Phys. Rev. Lett.* **126**, 040603 (2021).
- [10] Y. Lahini, R. Pugatch, F. Pozzi, M. Sorel, R. Morandotti, N. Davidson, and Y. Silberberg, Observation of a localization transition in quasiperiodic photonic lattices, *Phys. Rev. Lett.* **103**, 013901 (2009).
- [11] C. Tang and M. Kohmoto, Global scaling properties of the spectrum for a quasiperiodic Schrödinger equation, *Phys. Rev. B* **34**, 2041 (1986).
- [12] H. Hiramoto and M. Kohmoto, Scaling analysis of quasiperiodic systems: Generalized Harper model, *Phys. Rev. B* **40**, 8225 (1989).
- [13] A. Jagannathan, The Fibonacci quasicrystal: Case study of hidden dimensions and multifractality, *Rev. Mod. Phys.* **93**, 045001 (2021).
- [14] X. Li, X. Li, and S. D. Sarma, Mobility edges in one-dimensional bichromatic incommensurate potentials, *Phys. Rev. B* **96**, 085119 (2017).
- [15] H. Yao, A. Khoudli, L. Bresque, and L. Sanchez-Palencia, Critical behavior and fractality in shallow one-dimensional quasiperiodic potentials, *Phys. Rev. Lett.* **123**, 070405 (2019).
- [16] H. Yao, T. Giamarchi, and L. Sanchez-Palencia, Lieb-Liniger bosons in a shallow quasiperiodic potential: Bose glass phase and fractal Mott lobes, *Phys. Rev. Lett.* **125**, 060401 (2020).
- [17] D. Tanese, E. Gurevich, F. Baboux, T. Jacqmin, A. Lemaître, E. Galopin, I. Sagnes, A. Amo, J. Bloch, and E. Akkermans, Fractal energy spectrum of a polariton gas in a Fibonacci quasiperiodic potential, *Phys. Rev. Lett.* **112**, 146404 (2014).

- [18] D. Hofstadter, Energy levels and wave functions of Bloch electrons in rational and irrational magnetic fields, *Phys. Rev. B* **14**, 2239 (1976).
- [19] K. Madsen, E. Bergholtz, and P. Brouwer, Topological equivalence of crystal and quasicrystal band structures, *Phys. Rev. B* **88**, 125118 (2013).
- [20] J. Fraxanet, U. Bhattacharya, T. Grass, D. Rakshit, M. Lewenstein, and A. Dauphin, Topological properties of the long-range Kitaev chain with Aubry-André-Harper modulation, *Phys. Rev. Res.* **3**, 013148 (2021).
- [21] J. Fraxanet, U. Bhattacharya, T. Grass, M. Lewenstein, and A. Dauphin, Localization and multifractal properties of the long-range Kitaev chain in the presence of an Aubry-André-Harper modulation, *Phys. Rev. B* **106**, 024204 (2022).
- [22] J. Wang, X.-J. Liu, G. Xianlong, and H. Hu, Phase diagram of a non-Abelian Aubry-André-Harper model with  $p$ -wave superfluidity, *Phys. Rev. B* **93**, 104504 (2016).
- [23] Q.-B. Zeng, S. Chen, and R. Lü, Generalized Aubry-André-Harper model with  $p$ -wave superconducting pairing, *Phys. Rev. B* **94**, 125408 (2016).
- [24] M. Saha, S. Maiti, and A. Purkayastha, Anomalous transport through algebraically localized states in one dimension, *Phys. Rev. B* **100**, 174201 (2019).
- [25] T. Liu, P. Wang, S. Chen, and G. Xianlong, Phase diagram of a generalized off-diagonal Aubry-André model with  $p$ -wave pairing, *J. Phys. B: At. Mol. Opt. Phys.* **51**, 025301 (2018).
- [26] Y. Wang, Y. Wang, and S. Chen, Spectral statistics, finite-size scaling and multifractal analysis of quasiperiodic chain with  $p$ -wave pairing, *Eur. Phys. J. B* **89**, 254 (2016).
- [27] M. Yahyavi, B. Hetényi, and B. Tanatar, Generalized Aubry-André-Harper model with modulated hopping and  $p$ -wave pairing, *Phys. Rev. B* **100**, 064202 (2019).
- [28] F. Krausz and M. Ivanov, Attosecond physics, *Rev. Mod. Phys.* **81**, 163 (2009).
- [29] F. Calegari, G. Sansone, S. Stagira, C. Vozzi, and M. Nisoli, Advances in attosecond science, *J. Phys. B: At. Mol. Opt. Phys.* **49**, 062001 (2016).
- [30] E. Goulielmakis and T. Brabec, High harmonic generation in condensed matter, *Nat. Photon.* **16**, 411 (2022).
- [31] E. Constant, D. Garzella, P. Breger, E. Mével, C. Dorrer, C. Le Blanc, F. Salin, and P. Agostini, Optimizing high harmonic generation in absorbing gases: Model and experiment, *Phys. Rev. Lett.* **82**, 1668 (1999).
- [32] J. R. Sutherland, E. Christensen, N. Powers, S. Rhynard, J. Painter, and J. Peatross, High harmonic generation in a semi-infinite gas cell, *Opt. Express* **12**, 4430 (2004).
- [33] J. Li, J. Lu, A. Chew, S. Han, J. Li, Y. Wu, H. Wang, S. Ghimire, and Z. Chang, Attosecond science based on high harmonic generation from gases and solids, *Nat. Commun.* **11**, 2748 (2020).
- [34] T. T. Luu, Z. Yin, A. Jain, T. Gaumnitz, Y. Pertot, J. Ma, and H. J. Wörner, Extreme-ultraviolet high-harmonic generation in liquids, *Nat. Commun.* **9**, 3723 (2018).
- [35] O. Neufeld, Z. Nourbakhsh, N. Tancogne-Dejean, and A. Rubio, *Ab initio* cluster approach for high harmonic generation in liquids, *J. Chem. Theory Comput.* **18**, 4117 (2022).
- [36] A.-W. Zeng and X.-B. Bian, Impact of statistical fluctuations on high harmonic generation in liquids, *Phys. Rev. Lett.* **124**, 203901 (2020).
- [37] S. Ghimire, A. D. DiChiara, E. Sistrunk, P. Agostini, L. F. DiMauro, and D. A. Reis, Observation of high-order harmonic generation in a bulk crystal, *Nat. Phys.* **7**, 138 (2011).
- [38] G. Ndashimiye, S. Ghimire, M. Wu, D. A. Browne, K. J. Schafer, M. B. Gaarde, and D. A. Reis, Solid-state harmonics beyond the atomic limit, *Nature (London)* **534**, 520 (2016).
- [39] J.-B. Li, X. Zhang, S.-J. Yue, H.-M. Wu, B.-T. Hu, and H.-C. Du, Enhancement of the second plateau in solid high-order harmonic spectra by the two-color fields, *Opt. Express* **25**, 18603 (2017).
- [40] D. Bauer and K. K. Hansen, High-harmonic generation in solids with and without topological edge states, *Phys. Rev. Lett.* **120**, 177401 (2018).
- [41] H. Jürß and D. Bauer, High-harmonic generation in Su-Schrieffer-Heeger chains, *Phys. Rev. B* **99**, 195428 (2019).
- [42] N. Baldelli, U. Bhattacharya, D. González-Cuadra, M. Lewenstein, and T. Graß, Detecting Majorana zero modes via strong field dynamics, *ACS Omega* **7**, 47424 (2022).
- [43] J. Alcalà, U. Bhattacharya, J. Biegert, M. Ciappina, U. Elu, T. Graß, P. T. Grochowski, M. Lewenstein, A. Palau, T. P. H. Sidiropoulos, T. Steinle, and I. Tyulnev, High-harmonic spectroscopy of quantum phase transitions in a high- $T_c$  superconductor, *Proc. Natl. Acad. Sci. USA* **119**, e2207766119 (2022).
- [44] M. L. Bera, J. O. de Almeida, M. Dziurawiec, M. Płodzień, M. M. Maška, M. Lewenstein, T. Grass, and U. Bhattacharya, Topological phase detection through high-harmonic spectroscopy in extended Su-Schrieffer-Heeger chains, *Phys. Rev. B* **108**, 214104 (2023).
- [45] A. Pattanayak, Á. Jiménez-Galán, M. Ivanov, and G. Dixit, High harmonic spectroscopy of disorder-induced Anderson localization, [arXiv:2101.08536](https://arxiv.org/abs/2101.08536).
- [46] G. Jose, R. Malla, V. Srinivasan, A. Sharma, and S. Gangadharaiah, Phase diagram for the Harper model of the honeycomb lattice, *J. Phys.: Condens. Matter* **30**, 385603 (2018).
- [47] K. Drese and M. Holthaus, Phase diagram for a modified Harper model, *Phys. Rev. B* **55**, R14693 (1997).
- [48] H. Hiramoto and M. Kohomoto, Electronic spectral and wavefunction properties of one-dimensional quasiperiodic systems: A scaling approach, *Int. J. Mod. Phys. B* **06**, 281 (1992).
- [49] G. Orlando, C.-M. Wang, T.-S. Ho, and S.-I. Chu, High-order harmonic generation in disordered semiconductors, *J. Opt. Soc. Am. B* **35**, 680 (2018).
- [50] A. Chhabra and R. V. Jensen, Direct determination of the  $f(\alpha)$  singularity spectrum, *Phys. Rev. Lett.* **62**, 1327 (1989).
- [51] E. Cuevas, Multifractality of Hamiltonians with power-law transfer terms, *Phys. Rev. B* **68**, 184206 (2003).
- [52] J. W. Kantelhardt, S. A. Zschiegner, E. Koscielny-Bunde, S. Havlin, A. Bunde, and H. Stanley, Multifractal detrended fluctuation analysis of nonstationary time series, *Physica A* **316**, 87 (2002).
- [53] S. Ganeshan, J. H. Pixley, and S. Das Sarma, Nearest neighbor tight binding models with an exact mobility edge in one dimension, *Phys. Rev. Lett.* **114**, 146601 (2015).
- [54] X. Cai and Y.-C. Yu, Exact mobility edges in quasiperiodic systems without self-duality, *J. Phys.: Condens. Matter* **35**, 035602 (2023).

- [55] R. J. Bell and P. Dean, Atomic vibrations in vitreous silica, *Discuss. Faraday Soc.* **50**, 55 (1970).
- [56] Z. Guan, X.-X. Zhou, and X.-B. Bian, High-order-harmonic generation from periodic potentials driven by few-cycle laser pulses, *Phys. Rev. A* **93**, 033852 (2016).
- [57] M. Schreiber and H. Grussbach, Multifractal wave functions at the Anderson transition, *Phys. Rev. Lett.* **67**, 607 (1991).
- [58] D. Shechtman, I. Blech, D. Gratias, and J. W. Cahn, Metallic phase with long-range orientational order and no translational symmetry, *Phys. Rev. Lett.* **53**, 1951 (1984).
- [59] S. Carr, D. Massatt, S. Fang, P. Cazeaux, M. Luskin, and E. Kaxiras, Twistronics: Manipulating the electronic properties of two-dimensional layered structures through their twist angle, *Phys. Rev. B* **95**, 075420 (2017).
- [60] Z. Hennighausen and S. Kar, Twistronics: A turning point in 2D quantum materials, *Electron. Struct.* **3**, 014004 (2021).
- [61] Y. Cao, V. Fatemi, S. Fang, K. Watanabe, T. Taniguchi, E. Kaxiras, and P. Jarillo-Herrero, Unconventional superconductivity in magic-angle graphene superlattices, *Nature (London)* **556**, 43 (2018).